Available online at www.sciencedirect.com

ScienceDirect

Procedia Engineering 00 (2017) 000–000

Procedia Engineering

www.elsevier.com/locate/procedia

International High- Performance Built Environment Conference – A Sustainable Built Environment Conference 2016 Series (SBE16), iHBE 2016

The effect of building facades on outdoor microclimate – dependence model development using terrestrial thermography and multivariate analysis

Jonathan Fox[a,b]*, Natalya De Pooter[a]

[a]*Faculty of Built Environment, The University of New South Wales (UNSW), Sydney NSW 2052, Australia*
[b]*CRC for Low Carbon Living Ltd, Tyree Energy Technology Building - UNSW, Sydney NSW 2052, Australia*

Abstract

This paper describes ground-based thermal infrared (TIR) data collection and the development of a multivariate regression model to predict brightness surface temperature from thermal images. The statistical model estimates surface temperature regressed against thermal image red, green and blue (RGB) values with high predictive strength ($R^2 = 0.992$) for later multi-image stitching and facet-scale spatio-temporal analyses within a Geographical Information Systems (GIS) environment.

Peer-review under responsibility of the organizing committee iHBE 2016.

Keywords: Urban microclimate; building facades; ground-based remote sensing; infrared thermography; multivariate regression

1. Introduction

The radiative, thermal, moisture and aerodynamic properties of urban surfaces alter the fundamental energy, mass and momentum exchanges that produce distinct urban climates directly contributing to the urban heat island (UHI) effect [1]. Below mean roof level within the urban canopy layer (UCL) exchange processes operating on urban surfaces at different microscales ($<10^2$m) generate unique microclimates each of which is strongly influenced by the intrinsic properties of the surface and the morphology of its immediate surroundings [1,2]. Efforts to mitigate urban heating and improve outdoor thermal comfort have focused on alterations to surface thermal and radiative properties,

* Corresponding author. Tel.: +61 (02) 9385 5247; Mob.: +61 (0) 408 022 788.
E-mail address: jonathan.fox@unsw.edu.au

Peer-review under responsibility of the organizing committee iHBE 2016.

facet geometry, moisture availability and urban form with the aim of quantifying and predicting changes to the physical processes that influence urban climates across relevant temporal and spatial scales [3,4].

Advances in aerial and satellite remote hyperspectral and LiDAR platforms have enabled surface mapping for local and canyon-scale climatology [5,6]. However, thermo-spatial mapping and the development of appropriate visualization, diagnostic and predictive tools for investigating surface-atmosphere exchange at the "architectural" scale (~10^0m to ~10^1m) – where individual buildings are considered to be the fundamental units to create the urban climate [4] – remain underdeveloped yet have the potential to enhance micrometeorological observation, surface thermal specification [7] and the optimization of decision-making for sustainable cities [8].

Surface temperature is of prime importance in urban microclimatology [9]. At any given location surface temperature is controlled by the surface's surface energy balance (SEB) [10]. Surface temperature is fundamentally related to each non-solar component flux of the surface's SEB [11] and directly controls surface long-wave (infrared) radiation emission [12]. Once known, the temperature of an urban surface may be used to derive surface thermal properties (e.g. emissivity) and radiative fluxes [13]. However, remotely sensed urban surface temperatures, which are derived from emitted thermal infrared radiation, are indirectly measured and relating the observed signal to the emitting surface is a key challenge [9,14] prone to numerous methodological pitfalls including sensor calibration errors, atmospheric effects, non-blackbody emissivity and thermal anisotropy at local scales [15,16].

This research addresses a gap in ground-based microclimate observations at the building scale and describes one part of the development of a novel mixed-method approach to quantify the effects of building facades on microclimate using a combination of ground-based remote sensors, field measurements, aerial and in-situ spatial data and statistical analysis managed in a geographical information systems (GIS) environment. The aim of the research is to improve understanding of the microclimate effects of building facades and to develop a planning application to predict facade surface temperatures under various architectural design and canyon geometry scenarios with a high confidence level in order to enhance climate-sensitive design. This paper describes the thermal infrared (TIR) data collection and the development of a multivariate regression model to derive "brightness" surface temperature from thermal images.

2. Materials and methods

2.1. Study area

Summer daytime data were collected for 61 multi-storey buildings located in metropolitan Sydney between late-December 2015 and mid-March 2016. Sydney is located on the east coast of Australia at latitude 33° 51′ S and has a temperate climate with typically mild winters and dry, warm summers [17]. Sydney is the largest and most densely populated city in Australia with some inner-city suburbs, including Pyrmont/Ultimo, Potts Point/Woolloomooloo, Darlinghurst and Surry Hills exceeding 13 000 people per square kilometer [18]. Of the 61 buildings surveyed 97% were residential flat buildings and the mean effective facade height was 18.5m.

2.2. Data collection

In-situ data included ground-based remotely-sensed imagery and morphological data for the derivation of urban structure parameters (building form, canyon H/W, etc.). Ground-based images were obtained from 1.5m(h) tripod-mounted high-resolution thermal infrared (TIR) (7.5–13μm), multispectral (0.52-0.92μm) and visible-spectrum (0.4 -0.7μm) digital cameras. A FLIR B335 thermal camera was used to record facade surface temperature (refer Table 1 for IR camera specifications). The mean normal spatial resolution (pixel size) was 48mm at a target distance of 18.5m.

2.3. Basic principles of thermal infrared imaging

Thermal infrared cameras detect infrared radiation which is related to the object's surface temperature by Stefan-Boltzmann's Law [19]. Converting infrared radiation to temperature depends on the internal calibration of the camera which "automatically" deals with the complex relations expressed by Planck's Laws relative to a blackbody

[20,21]. Internal calibration converts the detected infrared radiation into raw digital counts to quantify radiance values that are, via an imaging algorithm, displayed as red, green and blue (RGB) colour "thermal" images corresponding to per-pixel temperature values [19,21].

The RGB colour assignment to temperature values is determined by the proprietary imaging algorithm with user control over colour palette and "colour distributions" (see below) to optimize thermal image display [21,22]. Since raw radiometric data recorded by the FLIR B335 camera were not readily available and only *per-image* per-pixel temperature values are recoverable from the camera manufacturer's proprietary software, an innovative method was developed to recover temperature measurements from image colour matrices for later multi-image stitching and spatio-temporal analyses using third-party software platforms.

To derive per-pixel surface temperature from an RGB "thermal" image (in JPEG format) the relationship between temperature values and RBG distributions was modeled using an ordinary least squares (OLS) statistical expression with 95% confidence interval and high predictive strength ($R^2 = 0.992$) as represented by the coefficient of determination (R^2) which measures the percentage of total variation in the dependent variable (surface temperature) explained by the regression model [23]. R^2 as a predictor of "goodness of fit" or model success is well established [24]. The development of a "split linear" regression model to predict per-pixel surface temperature from RGB intensity counts is described in Sub-section 2.4 below.

Table 1. FLIR B335 thermal camera specifications.

Imaging and Optics Data for FLIR B335 Infrared (IR) Camera	
IR resolution	320 × 240 pixels (76 800)
Thermal sensitivity	< 0.05°C @ +30°C/50 mK
IR Measurement accuracy	±2°C or ±2% of reading
IR spectral range	7.5–13μm
Object temperature range	–20°C to +120°C
45° lens field of view (FOV)	45° x 33.8°
45° lens focal length (*f*)	9.66mm (nominal 10mm)
Instantaneous field of view (IFOV)	2.59 mrad
IR image frequency	30Hz
IR detector type	FPA uncooled microbolometer
Emissivity correction	0.01 to 1.0
Image storage format	Standard JPEG
Temperature data	CSV table data per pixel

Source: FLIR data sheet for camera B335 (30Hz) PN 45312-0201

2.4. Thermal data pre-processing routine in GIS environment

FLIR "Tools/Tools+" proprietary software enables the export of thermal image temperature data as a matrix of comma-separated values (.csv) [25]. The temperature matrix values match the corresponding per-pixel RGB values distributed in the thermal image. The proprietary software also enables the post-processing adjustment of the colour palette and "colour distribution" of the thermal image [25]. Three colour distributions are available that are intended primarily to facilitate visualisation. Preliminary curve-estimation of all three color distributions – to identify the most suitable statistical model to regress surface temperature against RGB values – produced lower coefficients of determination ($R^2 < 0.9$) for the alternative "histogram equalization" and "signal linear" options using an identical test model. The "temperature linear" (TL) colour distribution option was selected to display and save the RGB thermal images for final regression model development. The TL colour distribution displays colour information distributed linearly to per-pixel temperature values [25]. All statistical curve-estimation and modeling was performed using the software package IBM SPSS Statistics 22.

Once the colour distribution was set to TL and all thermal images were equalised to the same temperature scale of interest using auto-adjust in FLIR Tools/Tools+, the RGB colour images and the .csv files were imported into ArcGIS (Esri) for further processing. Individual RGB colour matrices (raster datasets) were generated each consisting of 320 x 240 cells (columns x rows) of RGB values in the range 0-255 for each band. Unwanted elements in the image scene (e.g. cars, logos and temperature scale bar) were masked in ArcMap prior to single band raster layer creation and automatically assigned a "no value" of -9999 when exported as an ASCII file for later conversion from table to column format. All table data was converted to column format via a batch routine in SPSS. Once the regression model was completed, the raster datasets (of the independent variables), which were created earlier in the routine, were then used to recover per pixel temperature values from thermal images using equations scripted in map algebra in the Raster Calculator toolset (with a conditional statement) in ArcMap. Figure 1 illustrates the workflow for image and data processing and final temperature recovery using ArcGIS and other digital platforms.

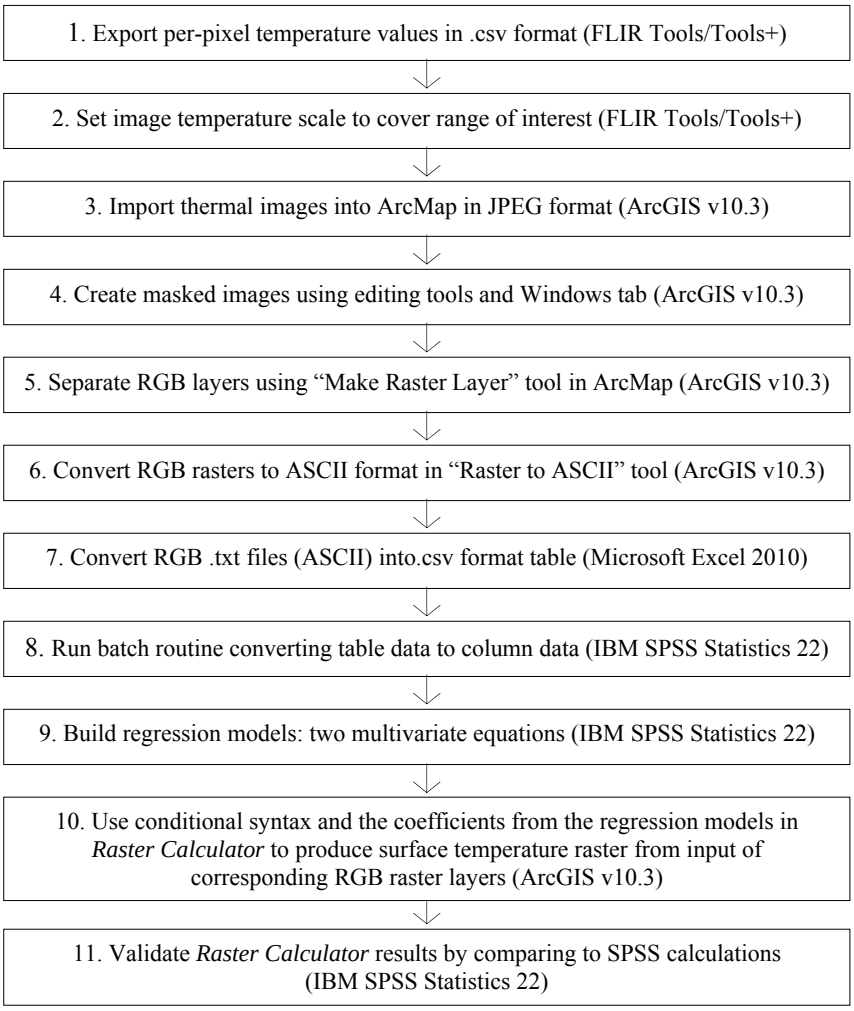

Fig. 1. workflow diagram for multivariate model development across digital platforms.

2.5. Description of split-linear statistical model derived from sample datasets

Per-pixel temperature and RGB values from four separate thermal image files were used to construct the model. The four images were chosen such that the lowest and highest temperatures across all images in the complete dataset were represented (after masking unwanted features). Across the sample set of pixels, the minimum temperature was

13.82°C and the maximum was 76.74°C. The final development dataset consisted of 275 471 pixels, each associated with a temperature, red, green and blue intensity value.

Figure 2 represents the relationship between the values of each component of RGB and the dependent variable, inverse of temperature, for red and green values (blue not shown) with the points plotted in the colour of the corresponding pixel. This illustrates the relationship between image colour and inverse of temperature and facilitated the identification of the inflection point value. The use of the inverse of the temperature will be discussed later.

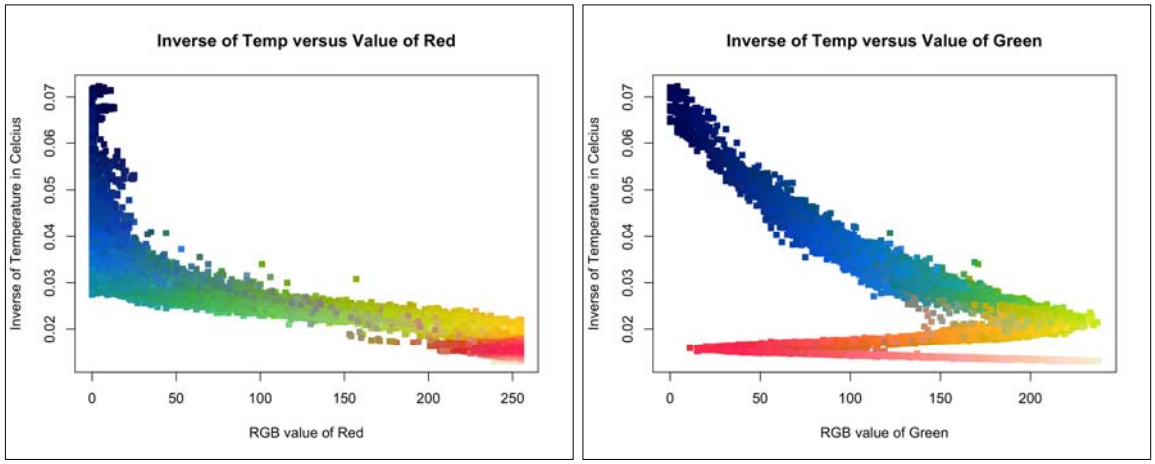

Fig. 2. (a) RGB value of red versus the inverse of temperature; (b) RGB value of green versus the inverse of temperature.

The plot of red was relatively linear against inverse temperature. However, the plots of green and blue (not shown) exhibit non-linearity as one value of blue or green could be associated with two different temperatures, depending on the RGB values of the other pixel colours. In the development of the model several combinations and transformations of the variables were tested. Additional predictive variables created included interaction terms and the squares and cubes of each component of the RGB (red squared, red cubed, etc.). Models using the inverse of the temperature as the dependent variable performed better (higher R^2) than models using temperature.

An important consideration in the model development was multi-collinearity. Multi-collinearity is the high variance of the model coefficient estimates which create instability of the coefficients. The variance inflation factor (VIF) was used to assess the multi-collinearity. From earlier curve-estimation it was evident that a single linear multivariate model exhibited multi-collinearity when acceptance thresholds were set at VIF < 10 and the Condition Index (CI) set at CI < 30 and considering other model factors [26]. The final model is a combination of two separate models. The blue and green curves were split into relatively linear sections conditional on a red value threshold (red < 175) corresponding to the inflection point. The VIF for each of the models are well within an acceptable range (Figure 3). R^2 for Model 1 is 0.981 and for Model 2 is 0.958 which indicates that for each model over 95% of the variation in the data is accounted for by the models (Table 2). The R^2 for the final model (i.e. the combination of the two separate models) is calculated from first principles. The resulting R^2 of 0.992 is higher than those for the individual models because the calculation used the overall average temperature rather than the average temperature of each subset when calculating the residuals.

Coefficients

Model		Unstandardized Coefficients		Standardized Coefficients	t	Sig.	Collinearity Statistics
		B	Std. Error	Beta			VIF
	(Constant)	.063	.000		2514.829		
	red2	9.099E-8	.000	.115	182.272	3.174	.315
	green	.000	.000	-1.353	-1652.836	5.329	.188
	blue	-2.717E-5	.000	-.323	-360.704	6.380	.157

Coefficients

Model		Unstandardized Coefficients		Standardized Coefficients	t	Sig.	Collinearity Statistics
		B	Std. Error	Beta			VIF
	(Constant)	.027	.000		1403.797		
	red	-4.135E-5	.000	-.461	-576.481	1.866	.536
	green3	3.446E-10	.000	.473	558.292	2.091	.478
	blue2	-2.089E-7	.000	-.255	-396.174	1.203	.831

Fig. 3. (a) Model 1 coefficients and collinearity statistics; (b) Model 2 coefficients and collinearity statistics.

Table 2. Model 1 (R<175) and Model 2 (R≥175) summary results.

Regression Model (Red value threshold)	R	R^2	Adjusted R^2	Std Error of the Estimate
Model 1 (R<175)	0.990	0.981	0.981	0.00093
Model 2 (R≥175)	0.979	0.958	0.958	0.00046

3. Results and discussion

3.1. Statistical model performance

The predicted temperature and the residuals were plotted against the recorded ("actual") temperature previously obtained from the original .csv temperature data (Figure 4).

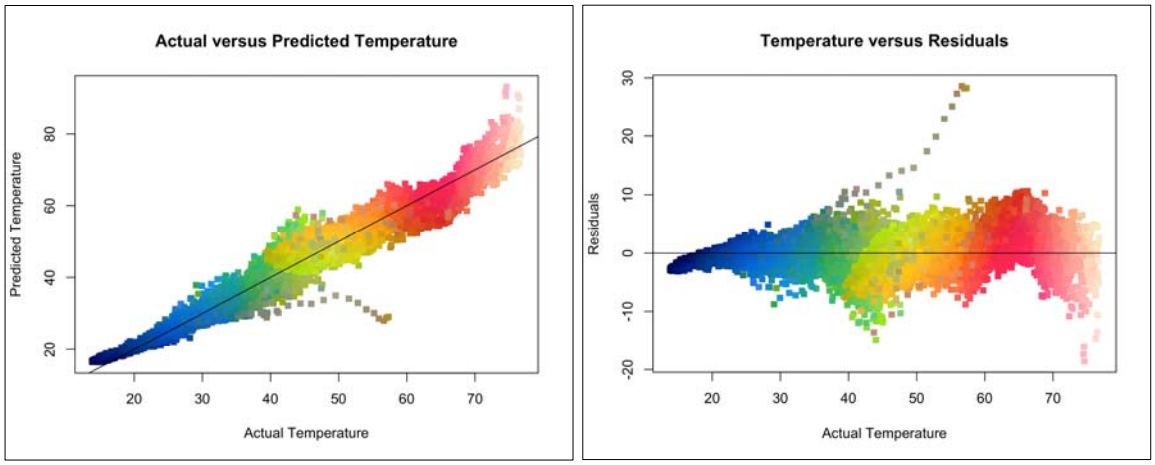

Fig. 4. (a) plot of predicted temperature against actual temperature; (b) plot of residuals against actual temperature.

The reference line in Figure 4(a) indicates where the predicted temperature is the same as the actual. The problematic grey pixels appear to have the greatest degree of error. This can also be seen in Figure 4(b) in the plot of residuals against actual temperature. The lower spread of blue points indicates a tighter model fit for lower temperatures. In Figure 4 the points are plotted on top of each other and do not readily show the concentration of residuals close to zero. The density of points close to zero is indicated by distributions of residuals (Figure 5), with 47.9% of the predictions within 0.5°C of the actual temperature, 75.1% within 1.0°C of the actual temperature, 90% within 1.68°C of the actual temperature and 95% of the predictions within 2.3°C of the actual temperature.

In order to validate that the model performs well on images that were not used in the development model, temperatures were predicted for two additional images. For the validation images, 47.1% of the predictions were within 0.5°C of the actual temperature, 73.5% were within 1.0°C of the actual temperature, 90% were within 1.81°C of the actual temperatures and 95% were within 2.49°C of the actual temperature, confirming near equivalence in distribution of residuals when compared to the model (Figure 5). The variation in the distributions of residuals between model and validation data may be due to null pixels (logos, temperature scale bar, etc.) that were not masked or temperature values outside the set temperature range which should have been masked.

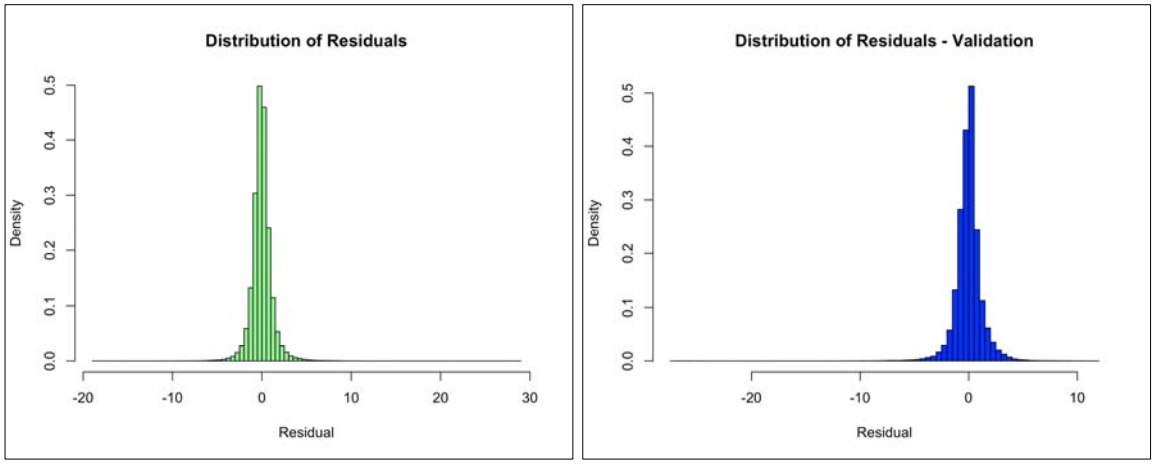

Fig. 5. (a) histogram distribution of residuals for model; (b) histogram distribution of residuals for validation.

3.2. Statistical model limitations

For a perfect model each RGB value should map to a unique temperature. However a perfect one-to-one mapping of RGB colour to temperature was not possible with the development data for the following reasons:

- A set of greyish coloured points (Figure 2) that appear to have a systematic pattern but are inconsistent with other points for similar temperatures. Possible causes for this include sections of the image (e.g. logos, etc.) that have not been masked or smoothing of the image by the instrument (infrared camera).
- The spread of the cloud of points around the line (Figure 4(a)) which suggests that more than one temperature is represented by the same RGB value. The distribution of the range of temperatures having the same RGB value was quantified with 54.1% of RGB values corresponding to a single temperature and the remaining 45.9% of RGB values corresponding to more than one temperature. However, only 4.4% of the RGB colours represent temperatures that have a maximum difference of more than 2^{o}C and 55.6% of the RGB colours represent temperatures that span less than or equal to 0.05^{o}C.

3.3. Discussion

High spatial resolution ground-based thermography supplements the coarser scale and birds-eye-view limitations of aerial and satellite thermal platforms [12] potentially providing new information about the thermal, spatial and temporal characteristics of urban vertical surfaces and the complete urban surface temperature [15]. Mapping temperature to the surface of interest and the recovery of temperature data from thermal images are important steps to quantify the spatial distribution of surface temperature [15,27]. However, thermographs are typically displayed as RGB colour images. The RGB colour assignment to temperature is encoded within a proprietary imaging algorithm that limits the straightforward recovery of per-pixel temperature values from RGB "thermal" images [22]. The method described above statistically models the dependency between temperature and per-pixel RGB values with a high confidence level (R^2 = 0.992), high concentration of residuals close to zero (as evidenced by 90% of residuals being within 1.68^{o}C of actual temperatures) and high repeatability (subject to quality of data pre-processing). Once developed, the regression model enables the relatively straightforward retrieval of (brightness) temperatures from single or mosaiced RGB thermal images within a GIS-based environment.

The application of the statistical model to temperature recovery from thermal images of building facades has some advantages over previous methods identified in the literature. Prior methods for the recovery of temperature from thermographs commonly use texture mapping, a process of mapping surface texture onto a three-dimensional model [15,28]. This approach uses laser-scanning and survey equipment and the time-consuming independent

generation and then coregistration of the 3D-building model and thermal texture maps. City-wide, multi-site application of this approach has not been identified in the literature and would likely face significant logistical and economic constraints. Since the focus of this research is the effect of facades on outdoor microclimate in the canyon, a simple 2D planar rather than 3D representation of the facade surface is assumed for non-complex facades. This assumption holds since surface materials, surface orientation and canyon structure dominate radiative effects at the scale of interest (~10^0m to ~10^1m) [7,29,30]. In this case, standard single image rectification using plane projective transformation and mosaicking software may be used [31]. Once the thermal image has been geometrically corrected and then registered to the real building (object) coordinate system using GIS-based routines the resulting thermographic orthomosaic is a georeferenced product ready for conventional analysis in a GIS-based environment

The methodology proposed here exploits the relative efficacy of RGB colour image orientation, notwithstanding the challenges presented by limited field of view (FOV) and lower image resolution of terrestrial thermal cameras [27]. These limitations are minimized due to the relatively short target distances (mean 18.5m), greater image resolution (mean normal IFOV of 48mm) and colour visualisation which aids feature differentiation during manual image orientation even for limited-texture surfaces [32]. Workflow flexibility may also be advantageous compared to existing GIS-based methods. For example, the mapping of per-pixel temperature data within 16-bit greyscale raster images [27] encodes brightness temperature at commencement and may limit straightforward corrections later in the workflow for angle, distance, view factor and emissivity effects which impact temperature accuracy [15]. The statistical method proposed here has the advantage of flexibility as to when corrections are applied in response to the availability of geometric, spatial and material data.

Some limitations in the statistical modelling have been previously identified (Sub-section 3.2). However, the relationship between the IR camera “noise equivalent temperature difference” (NETD), or thermal sensitivity (0.05^{o}C from Table 1), and model temperature variance per RGB value (refer Sub-section 3.2) requires further investigation in light of the sensitivity of NETD to surface temperature [19,22]. Application of the statistical model to temperature retrieval from thermal images of building facades must resolve limitations in orthomosaicing which result from the assignment of RGB colour values to the overlapping zones as the mean of neighbouring pixels or by preferential view direction [31]. This may impact temperature recovery accuracy unless prior RGB value adjustments are undertaken. Potential user errors in manual image orientation and tie point identification with low resolution (due to limited FOV) and sub-optimal surface texture have also been identified [32]. The accuracy of the georeferencing of the thermal mosaic to a referenced base plan within GIS depends on the accuracy of the base plan shapefile and satisfactory selection of corresponding anchor points. Since these two datasets are not typically created for equivalent end-purposes and level of detail (LOD), limitations in correspondence may impact registration accuracy. Finally, the assumption of plane uniformity for non-complex facades may limit the application of this method when investigating non-trivial 3D structures.

4. Conclusion

The lack of readily available commercial software platforms and standardised methods to map and model the surface temperature of building facades and the orientation challenges of using narrow FOV terrestrial thermography have been previously identified [27]. Texture mapping using photogrammetry or terrestrial laser scanners are common approaches to assigning surface thermal information to building models [15, 28]. However, these approaches have high equipment and time costs and have only been applied to limited sites. The method described here enables city-wide mapping of non-complex facades and the generation of a georeferenced thermal product ready for conventional analysis in a GIS-based environment. The growing availability of greater LOD mapping products may also improve the registration of the thermal orthomosaic to referenced base maps. Refinement of the statistical model for the recovery of accurate temperatures from thermal images may be possible with improved pre-processing (masking) and additional filtering of data based on the spread of residuals.

Acknowledgements

Research funding for this paper was provided by the Australian Cooperative Research Centre (CRC) for Low Carbon Living under Program 2 – "Low Carbon Precincts", Research Project RP2005 – Urban Micro Climates: Comparative study of major contributors to the Urban Heat Island effect in three Australian cities: Sydney, Melbourne, Adelaide.

References

[1] T.R. Oke, The energetic basis of the urban heat island, Quarterly Journal of the Royal Meteorological Society. 108,455 (1982) 1-24.
[2] T.R. Oke, Boundary Layer Climates, second ed., Methuen, New York, 1987.
[3] M. Santamouris and D. Kolokotsa (Eds.), Urban Climate Mitigation Techniques, Routledge, New York, 2016.
[4] H.A. Cleugh and C.S.B. Grimmond, Urban Climates and Global Climate Change, in: A. Henderson-Sellers and K. McGuffie (Eds.), The Future of the World's Climate, Elsevier, New York, 2012.
[5] Q. Weng, Remote sensing of impervious surfaces in the urban areas: Requirements, methods, and trends, Remote Sensing of the Environment. 117 (2012) 34-49.
[6] M. Irger, The Effect of Urban Form on Urban Microclimate, PhD Dissertation. University of New South Wales, Sydney, 2014.
[7] A. Christen, F. Meier and D. Scherer, High-frequency fluctuations of surface temperatures in an urban environment, Theoretical and Applied Climatology. 108,1-2 (2012) 301-324.
[8] K. Häb, N.H. Feige, L.S. Huettenberger, et al., Visualizing the temporal development of thermo-radiative features on ground-based thermographs, Environmental Earth Sciences. 72,10 (2014) 3781–3793.
[9] J.A. Voogt and T.R. Oke, Thermal remote sensing of urban climates, Remote Sensing of Environment. 86,3 (2003) 370-384.
[10] M. Roth, T. R. Oke and W. J. Emery, Satellite-derived urban heat islands from three coastal cities and the utilization of such data in urban climatology, International Journal of Remote Sensing. 10,11 (1989) 1699-1720.
[11] E.S. Krayenhoff and J.A. Voogt. A microscale three-dimensional urban energy balance model for studying surface temperatures." Boundary-Layer Meteorology. 123,3 (2007) 433-461.
[12] F. Meier, D. Scherer and J. Richters. Determination of persistence effects in spatio-temporal patterns of upward long-wave radiation flux density from an urban courtyard by means of Time-Sequential Thermography, Remote Sensing of Environment. 114,1 (2010) 21-34.
[13] T.R. Oke, The urban energy balance, Progress in Physical Geography. 22 (1988) 471-508.
[14] J.A. Voogt and T.R. Oke, Radiometric Temperatures of Urban Canyon Walls Obtained from Vehicle Traverses, Theoretical and Applied Climatology. 60,1-4 (1988) 199-217.
[15] C.A. Adderley, A. Christen and J.A. Voogt, The effect of radiometer placement and view on inferred directional and hemispheric radiometric temperatures of an urban canopy, Atmospheric Measurement Techniques Discussions. 8 (2015) 1891–1933.
[16] E. Parlow, R. Vogt and C. Feigenwinter, The urban heat island of Basel – seen from different perspectives, Die Erde (Journal of the Geographical Society of Berlin. 145,1-2 (2014) 96-110.
[17] Australian Bureau of Meteorology (BOM), Climate of Australia, Commonwealth of Australia, 2008.
[18] Australian Bureau of Statistics (ABS), Population Projections, Australia, 2012 to 2101, published 26 November 2013, available online: http://www.abs.gov.au/AUSSTATS/abs@.nsf/DetailsPage/3222.02012 (base) to 2101?OpenDocument.
[19] W. Minkina and S. Dudzik, Infrared thermography: errors and uncertainty, Wiley and Sons Ltd, UK, 2009.
[20] S.G. Burnay, T.L. Williams and C.H. Jones (Eds.), Applications of Thermal Imaging, Adam Hilger, Bristol, 1988.
[21] FLIR Systems AB, The Ultimate Infrared Handbook for R&D Professionals: A Resource Guide for Using Infrared in the Research and Development Industry, downloaded February 2014, available from from: http://www.flir.com/cs/apac/en/view/?id=42241.
[22] M. Vollmer and K-P. Mollman, Infrared Thermal Imaging Fundamentals, Research and Applications, Wiley, Hoboken, 2011.
[23] L.D. Schroeder, D.L. Sjoquist and P.E. Stephan, Understanding linear regression, SAGE Publications, Inc.,1986.
[24] N.J.D. Nagelkerke, A note on a general definition of the coefficient of determination, Biometrika. 78, 3 (1991) 691-692.
[25] FLIR Systems AB, FLIR Tools/Tools+ User's manual, FLIR Systems, Inc., accessed May 2016.
[26] R.M. O'Brien, A Caution Regarding Rules of Thumb for Variance Inflation Factors, Quality and Quantity. 41 (2007) 673–690.
[27] M. Previtali, S. Erba, E. Rosina, V. Redaelli, M. Scaioni and L. Barazzetti, Generation of a GIS-based environment for infrared thermography analysis of buildings, Proceedings of SPIE 8511 Infrared Remote Sensing and Instrumentation XX 85110U, (2012).
[28] M. Previtali, L. Barazzetti, V. Redaelli, M. Scaioni and E. Rosina, Rigorous procedure for mapping thermal infrared images on three dimensional models of building facades, Journal of Applied and Remote Sensing. 7,1 (2013) 1-19.
[29] M. Nunez and T.R. Oke, The energy balance of an urban canyon, Journal of Applied Meteorology. 16 (1977) 11-19.
[30] A. Hoyano, K. Asano and T. Kanamaru, Analysis of the sensible heat flux from the exterior surface of buildings using time sequential thermography, Atmospheric Environment. 33 (1999) 3941-3951.
[31] T. Luhmann and W. Tecklenburg, High-resolution image rectification and mosaicing – a comparison between panorama camera and digital camera, Proceedings of the ISPRS working group V/5, 'Panoramic Photogrammetry Workshop' Berlin, Germany 24-25 February 2005.
[32] M. Scaioni, E. Rosina, L. Barazzetti, M. Previtali and V. Redaelli, High resolution texturing of building facades with thermal images, Proceedings of SPIE 8354 Thermosense: Thermal Infrared Application XXXIV 835401, (2012) 1-12.